Multicomponent inverse scattering series internal multiple prediction Part II: Synthetic application

Jian Sun*, Kris Innanen*, Daniel Trad*, Yu Geng*

ABSTRACT

Identifying lower-higher-lower relationship is essential to inverse scattering series internal multiple prediction, which is more difficult for multicomponent predictions due to the wave-mode conversion of P- and S-waves. Since only conversions happened in the top layer can be handled by the algorithm, the input preparation for elastic internal multiple prediction becomes to an intractable problem. In paper of part I, we analytically analyzed the advantages and defects of input preparation using different methods, elastic stolt-migration, vertical traveltime stretching, and best-fitting velocity obtained by high resolution radon transform. In this paper, to examine the conclusions indicated previously, a synthetic model is utilized to implemented the multicomponent internal multiple prediction with different inputs generated by these approaches.

INTRODUCTION

In seismic exploration, internal multiples used to be identified as undesired noises because the conventional seismic imaging algorithms deal correctly only with primary reflections. One reason for its negative feedbacks is most of migration and inversion methods are based on the Born approximation, i.e., the assumption of one single scattering. By analyzing the role that primaries and multiples play in migration, recent studies indicate that, for a smooth and continuous velocity model, internal multiples will lead to an artificial, misleading , and false subsurface image (Berkhout and Verschuur, 2006; Behura et al., 2014; Zuberi and Alkhalifah, 2014; Li et al., 2016; Weglein, 2016). In practice, to enhance the image quality, internal multiples must be removed if we migrate seismic reflection in conventional way. It is worth to note that internal multiples has their unique characteristics, smaller reflection angle and longer ray-path, compared to primary events. These features of internal multiples recorded in seismic data could increase the aperture of illumination and enhance subsurface imaging and structure determination. In other words, instead of eliminating internal multiples in conventional imaging process, migration of internal multiples under appropriate imaging conditions could penetrate into earth to provide more stratigraphic information and to illuminate shadow zones where primaries cannot reach (Liu et al., 2011; Malcolm et al., 2009, 2011; Slob et al., 2014), for example, sub-salt areas. To make use of these attractive features, internal multiples prediction need to be performed precisely as multicomponent acquisition developed.

Considerable progress of internal multiple prediction has been made recently. There are two distinguished ways to attenuate internal multiples from primary events. One is transforming internal multiples to be 'surface-related' and then eliminating them by their characteristics of the free surface. The representative approach, boundary-related/layer-related method, by recalibrating and exfoliating the top of the multiple generators in a

*University of Calgary, CREWES Project

stepwise way, was implemented in different domains, such as in poststack (CMP) data (Kelamis et al., 2002), in common-focus-point (CFP) domain (Berkhout and Verschuur, 2005; Berkhout, 2006), in inverse-data domain (Luo et al., 2007). The second, by considering internal multiples as the combination of a certain sub-events based on the inverse scattering series, is optimal to implement the internal multiple prediction without any subsurface information in an automatic way. Weglein et al. (1997) demonstrated that internal mutliples can be estimated from sub-events which satisfy the lower-higher-lower criterion in the pseudo-depth or vertical traveltime domain. Many incentive research and discussions of inverse scattering series (ISS) on internal multiples prediction (IMP) have been presented serving diverse purposes. To correct the predicted amplitude of internal multiples and avoid the deterioration of the energy minimization adaptive subtraction, Zou and Weglein (2015) demonstrated an alternative version of ISS-IMP algorithm for all first order internal multiples in model of parameters varying in depth only. One of the key features to determine the capacity of the existing ISS-IMP algorithm in complex environments, is the search parameter selection which guarantees the selected combination to meet the lower-higher-lower relationship (Luo et al., 2007; Sun and Innanen, 2016b). To mitigate the artifacts of a fixed search parameter and to enhace the proximity of ISS algorithm, by reformulating ISS algorithm, Innanen (2017) demonstrated that inverse scattering-based internal multiple prediction can be performed with a non-stationary search parameter in time-related domains. Another promising line of research is to seek optimum domains in which apply to a relative stationary parameter. In particular, especially concerning artifact mitigation, implementation in $\tau - p$ domain (Coates and Weglein, 1996) appears to have some attractive features (Sun and Innanen, 2015) and motivates a numerical analysis of 2D ISS internal multiple prediction in couple plane-wave domain which has a range of attractive features, practical and computational (Sun and Innanen, 2016c). Moreover, the multidimensional plane-wave-domain ISS algorithm can also be merged with non-stationary parameter to perform 2D/3D application with time-varying parameter in challenging environments.

Nevertheless, these approaches, even though powerful, are on the strength of acoustic assumption which is not reality and consistent with rapidly developed multicomponent acquisition. For inverse scattering-based approach, unlike acoustic cases, wave-mode conversion in multicomponent seismic record will wreck the wavenumber / slowness - dependent relationship of sub-sevents in the combination and misleads the lower-higher-lower criteria. To adapt for multicomponent seismic records, by considering an isotropic-elastic-homogeneous background and decomposing the elastic inverse scattering series into types of wave-mode, Sun and Innanen (2016a) extend the elastic internal multiple prediction algorithm into 3D based on inverse scattering series, first introduced by Matson (1997), while involving wave-mode conversion.

However, preparing input for the multicomponent prediction algorithm, either proposed in pseudo-depth domain/horizontal slowness pseudo-depth domain, or plane wave domain, without causing suspicious noises and breaking lower-higher-lower relationship, is a key feature and remains to be an obstacle. Since the elastic inverse scattering series internal multiple algorithm only handles the wave-model conversion in the top layer, the reflections generated by same interface will be mislead and create aliasing combinations satisfying lower-higher-lower relationship. Based on the analytical analysis of input preparation illustrated in paper Part I, in this paper, we performed the multicomponent prediction on a

synthetic model with the inputs generated by different approaches.

PREDICTION FORMULATION: 1.5D CASE

$k-z$ domain algorithm

For layered cases, we have, $k_{x_s}^P = k_{x_g}^P = k_{x_g}^{SV}$ with P-wave source only, and $k_{x_s}^{SV} = k_{x_g}^{SV} = k_{x_g}^P$ with S-wave source only. Assume $z_s = z_g$, the prediction algorithm for a layered case can be simplified as,

$$\begin{aligned} b_3^{ij}(k_g,\omega) = -\int_{-\infty}^{+\infty} \mathrm{d}z_1 e^{\mathrm{i}(\nu^m+\nu^i)z_1} b_1^{im}(k_g,z_1) \int_{-\infty}^{z_1-\epsilon} \mathrm{d}z_2 e^{-\mathrm{i}(\nu^n+\nu^m)z_2} b_1^{mn}(k_g,z_2) \\ \times \int_{z_2+\epsilon}^{+\infty} \mathrm{d}z_3 e^{\mathrm{i}(\nu^j+\nu^n)z_3} b_1^{nj}(k_g,z_3) \end{aligned} \tag{1}$$

with vertical wavenumber written as,

$$\nu^X = \sqrt{\frac{\omega^2}{(c_0^X)^2} - (k_g^X)^2} \tag{2}$$

where, the input $b_1(k_g,z)$ is calculated as $b_1^{ij}(k_g,z) = \mathrm{i}2\nu^j D^{ij}(k_g,z)$, $\{i,j\} \in \{P,SV\}$. Here, j denotes the source side, and i represents the receiver side. $D^{ij}(k_g,z)$ is the migrated shot profile using elastic stolt migration in wavennumber manner with two constant background velocity for P- and SV-wave.

$p-z$ domain algorithm

Similar to acoustic cases, the prediction can also be transferred into horizontal-slowness pseudo-depth ($p-z$) domain by simply replacing the wavenumber variable. Its mathematical form is shown as,

$$\begin{aligned} b_3^{ij}(p_g,\omega) = -\int_{-\infty}^{+\infty} \mathrm{d}z_1 e^{\mathrm{i}(\nu^m+\nu^i)z_1} b_1^{im}(p_g,z_1) \int_{-\infty}^{z_1-\epsilon} \mathrm{d}z_2 e^{-\mathrm{i}(\nu^n+\nu^m)z_2} b_1^{mn}(p_g,z_2) \\ \times \int_{z_2+\epsilon}^{+\infty} \mathrm{d}z_3 e^{\mathrm{i}(\nu^j+\nu^n)z_3} b_1^{nj}(p_g,z_3) \end{aligned} \tag{3}$$

with vertical slowness written as,

$$q^X = \sqrt{\frac{1}{(c_0^X)^2} - (p_g^X)^2} \tag{4}$$

where, the input $b_1(p_g,z)$ is calculated as $b_1^{ij}(p_g,z) = \mathrm{i}2q^j D^{ij}(p_g,z)$, $\{i,j\} \in \{P,SV\}$. $D^{ij}(p_g,z)$ is migrated shot profile using elastic stolt migration in horizontal-slowness manner with two constant background velocity for P- and SV-waves.

$p-\tau$ domain algorithm

As delineated in paper of part I, the plane wave domain algorithm can be obtained by performing one-to-one mapping between pseudo-depth and vertical traveltime which requires a time-stretched $\tau - p$ transformed data as the inputs. However,to avoid interpolation process in time-stretching, we can also achieve the same goal by modifying the integral limits with a traditional $\tau - p$ transformed data as input. Therefore, hereinafter, multicomponent prediction with time-stretching method signifies the algorithm with time-stretched integral limits and will only be performed in this way. The 1.5D plane wave domain algorithm with time-stretching modified integral limits is shown as,

$$\begin{aligned} b_3^{ij}(p_g,\omega) = -\int_{-\infty}^{+\infty} \mathrm{d}\tau_1^{im} e^{\mathrm{i}\omega\tau_1^{im}} b_1^{im}(p_g,\tau_1^{im}) \int_{-\infty}^{\Upsilon(\tau_1^{im}|\tau_2^{mn})-\epsilon} \mathrm{d}\tau_2^{mn} e^{-\mathrm{i}\omega\tau_2^{mn}} b_1^{mn}(p_g,\tau_2^{mn}) \\ \times \int_{\Upsilon(\tau_2^{mn}|\tau_3^{nj})}^{+\infty} \mathrm{d}\tau_3^{nj} e^{\mathrm{i}\omega\tau_3^{nj}} b_1^{nj}(p_g,\tau_3^{nj}) \end{aligned} \tag{5}$$

where, the input $b_1(p_g,\tau)$ is obtained by $b_1^{ij}(p_g,\tau) = \mathrm{i}2q^j D^{ij}(p_g,\tau)$, $\{i,j\} \in \{P,SV\}$. $D^{ij}(p_g,\tau)$ is the linear transformation of shot profile. The modified integral limits is described as,

$$\Upsilon(\tau_2^{mn}|\tau_1^{nj}) = \begin{cases} \tau_2^{mn}, & j = m; \\ \frac{\alpha+\beta}{2\beta}\tau_2^{mn}, & j = S \;\&\; m = P; \\ \frac{2\beta}{\alpha+\beta}\tau_2^{mn}, & j = P \;\&\; m = S; \end{cases} \tag{6}$$

Besides the prediction with time-stretching in plane wave domain, the implementation can also be performed with the best-fitting velocity model to adapt the monotonicity condition of vertical traveltime and actual depth. With the best-fitting velocity model, the modified integral limits for the plane wave domain prediction algorithm is delineated as,

$$\Gamma(\tau_2^{mn}|\tau_1^{nj}) = \frac{v^{mn}(p_g,\tau_2^{mn})}{v^{nj}(p_g,\tau_1^{nj})}\tau_2^{mn} \tag{7}$$

where, v^{xy} is the best-fitting velocity model obtained by high-resolution hyperbolic radon transform.

By simply replacing $\Upsilon(\tau_2^{mn}|\tau_1^{nj})$ with $\Gamma(\tau_2^{mn}|\tau_1^{nj})$, the prediction algorithm with best-fitting velocity can be obtained. Based on the analytical analysis, we indicated in part I that prediction with best-fitting velocity model may requires a large research parameter. Because of the opposite sorting order of pseudo-depth, the multicomponent prediction with a cross-validate of vertical traveltime-stretching and best-fitting velocity model may allows a relative constant and smaller ϵ to identify the lower-higher-lower combinations.

SYNTHETIC: INPUT PREPARATION

A layered synthetic model containing two interfaces was build to generate shot profile and then implemented the elastic algorithm to predict all multiples in shot gather. The model parameters are delineated in Figure 1, from top to bottom, P-wave velocities are $[2000, 3500, 2500]m/s$, S-wave velocities are $[1200, 2000, 1300]m/s$, and densities are

$[1.5, 2.25, 1.6] g/cm^3$. A P-wave source is located in the middle of the model, and receivers in 4m interval are arranged at same level of depth. With four absorbing boundaries (dashed line in the model shown in Figure 1), a multi-component shot gather is generated using finite difference, i.e., only primaries and elastic internal multiples appear in the seismic record.

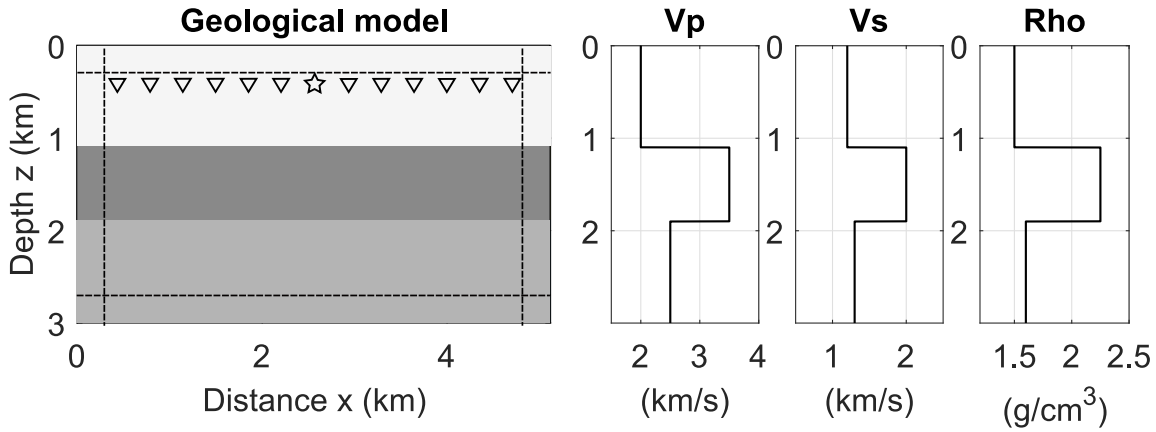

FIG. 1. Geological model and model parameters. The left panel shows a three layers geological model, the right panels indicate model parameters for P-, S-wave velocities, and density. From top to bottom, $v_p = [2.0, 3.5, 2.5]$ in km/s, $v_s = [1.2, 2.0, 1.3]$ in km/s, $\rho = [1.5, 2.25, 1.6]$ in g/cm^3.

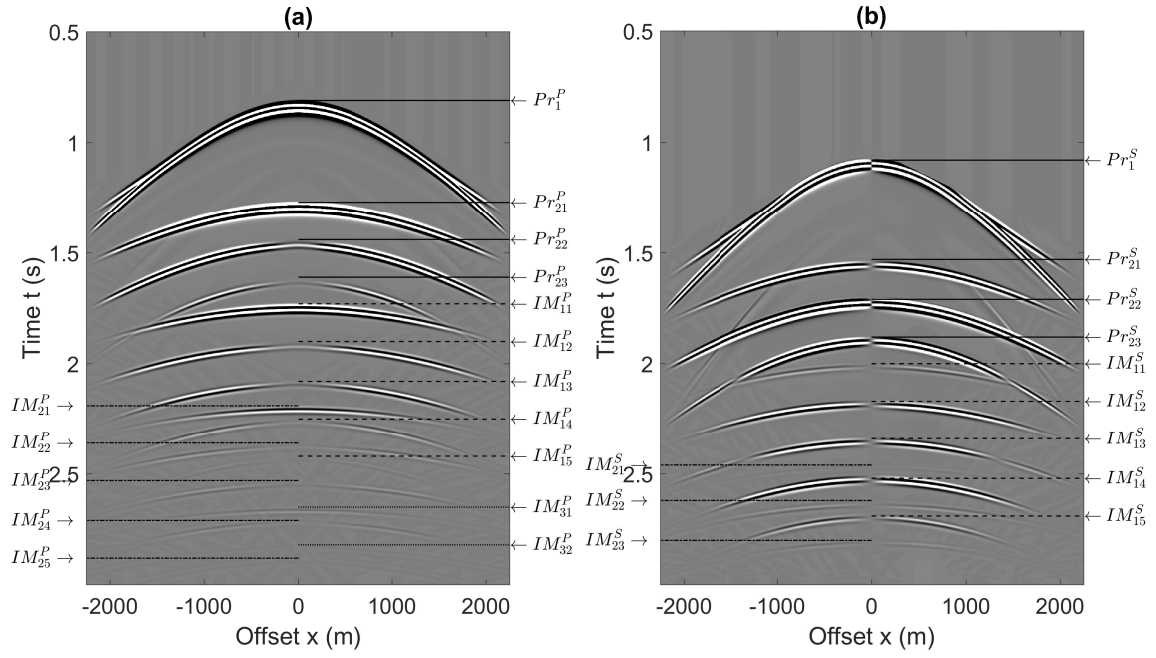

FIG. 2. *Helmholtz's* decomposition of shot profile. (a) P-wave component of the shot profile. (b) SV-wave component of the shot profile. Pr denote primary events, which are indicated by solid lines. IM represent the internal multiples. The 1st-order internal multiples are indicated by dashed lines. The second-order of them are indicated by dashed-dotted lines. The third-order of them are indicated by dotted lines. The details of annotations for all events are illustrated in Table 1.

After collected the shot profile, it is decomposed into P- and SV-wave component using *Helmholtz's* method. The decomposed P- and S-wave components of data are illustrated

in Figure 2, with all reflection events labelled. As noted, the amplitude polarity is symmetric over zero-offset in decomposed P-wave component, and is reversed over zero-offset in decomposed S-wave component. In Figure 2, both for P- and S-wave components, Pr denotes primaries, and IM represents all internal multiples. All primary events are indicated by solid lines. All 1st-order internal multiples are indicated by dashed lines, the dashed-dotted lines delineate all 2nd-order internal multiples , and the 3rd-order of them are labelled by dotted lines. The details of annotations for all reflection events are shown in Table 1.

Label-P	Primaries in P-mode	Label-S	Primaries S-mode
Pr_1^P	$\grave{P}\acute{P}$	Pr_1^S	$\grave{P}\acute{S}$
Pr_{21}^P	$\grave{P}\grave{P}\acute{P}\acute{P}$	Pr_{21}^S	$\grave{P}\grave{P}\acute{P}\acute{S}$
Pr_{22}^P	$\grave{P}\grave{P}\acute{S}\acute{P}$ & $\grave{P}\grave{S}\acute{P}\acute{P}$	Pr_{22}^S	$\grave{P}\grave{P}\acute{S}\acute{S}$ & $\grave{P}\grave{S}\acute{P}\acute{S}$
Pr_{23}^P	$\grave{P}\grave{S}\acute{S}\acute{P}$	Pr_{23}^S	$\grave{P}\grave{S}\acute{S}\acute{S}$
Label-P	1st-order IMs in P-mode	Label-S	1st-order IMs in S-mode
IM_{11}^P	$\grave{P}\grave{P}\acute{P}\grave{P}\acute{P}\acute{P}$	IM_{11}^S	$\grave{P}\grave{P}\acute{P}\grave{P}\acute{P}\acute{S}$
IM_{12}^P	$\grave{P}\grave{P}\acute{P}\grave{P}\acute{S}\acute{P}$	IM_{12}^S	$\grave{P}\grave{P}\acute{P}\grave{P}\acute{S}\acute{S}$
IM_{13}^P	$\grave{P}\grave{P}\acute{P}\grave{S}\acute{S}\acute{P}$	IM_{13}^S	$\grave{P}\grave{P}\acute{P}\grave{S}\acute{S}\acute{S}$
IM_{14}^P	$\grave{P}\grave{P}\acute{S}\grave{S}\acute{S}\acute{P}$	IM_{14}^S	$\grave{P}\grave{P}\acute{S}\grave{S}\acute{S}\acute{S}$
IM_{15}^P	$\grave{P}\grave{S}\acute{S}\grave{S}\acute{S}\acute{P}$	IM_{15}^S	$\grave{P}\grave{S}\acute{S}\grave{S}\acute{S}\acute{S}$
Label-P	2nd-order IMs in P-mode	Label-S	2nd-order IMs in S-mode
IM_{21}^P	$\grave{P}\grave{P}\acute{P}\grave{P}\acute{P}\grave{P}\acute{P}\acute{P}$	IM_{21}^S	$\grave{P}\grave{P}\acute{P}\grave{P}\acute{P}\grave{P}\acute{P}\acute{S}$
IM_{22}^P	$\grave{P}\grave{P}\acute{P}\grave{P}\acute{P}\grave{P}\acute{S}\acute{P}$	IM_{22}^S	$\grave{P}\grave{P}\acute{P}\grave{P}\acute{P}\grave{P}\acute{S}\acute{S}$
IM_{23}^P	$\grave{P}\grave{P}\acute{P}\grave{P}\acute{P}\grave{S}\acute{S}\acute{P}$	IM_{23}^S	$\grave{P}\grave{P}\acute{P}\grave{P}\acute{P}\grave{S}\acute{S}\acute{S}$
IM_{24}^P	$\grave{P}\grave{P}\acute{P}\grave{P}\acute{S}\grave{S}\acute{S}\acute{P}$		
IM_{25}^P	$\grave{P}\grave{P}\acute{P}\grave{S}\acute{S}\grave{S}\acute{S}\acute{P}$		
Label-P	3rd-order IMs in P-mode		
IM_{31}^P	$\grave{P}\grave{P}\acute{P}\grave{P}\acute{P}\grave{P}\acute{P}\grave{P}\acute{P}\acute{P}$		
IM_{32}^P	$\grave{P}\grave{P}\acute{P}\grave{P}\acute{P}\grave{P}\acute{P}\grave{P}\acute{S}\acute{P}$		

Table 1. The annotation of symbols shown in Figure 2. Here, Pr denotes primary events, IM denotes internal multiples. The superscript represent type of wave mode in received field. In the subscripts of primaries, the 1st number denotes related reflector, the 2nd number equals to number of S-wave path between the fist and last path plus one, i.e., Pr_{22}^P represent all events reflected by the second reflector involving one S-wave path between the first and last path, which are $\grave{P}\grave{P}\acute{S}\acute{P}$ & $\grave{P}\grave{S}\acute{P}\acute{P}$. In the subscripts of internal multiples, the 1st number denotes the order of internal multiples, the 2nd number also represents number of S-wave path between the first and last wave path.

In Table 1, the superscript delineates the wave-type. For primaries (Pr), the first number of subscript represents the corresponded reflector, the second number of subscript is related to the number of S-wave travel-path occurred in the current event, i.e., it equals to no.S-wave ray-path plus one in P-wave mode and equals to no.S-wave ray-path directly in S-wave mode. For instance, Pr_{22}^P is the primary event in P-wave component re-

flected by second reflector including two possible travel-path: $\grave{P}\grave{P}\acute{S}\acute{P}$ and $\grave{P}\grave{S}\acute{P}\acute{P}$, which involves one S-wave raypath and both of them are recorded at the same time (here, accents represent downgoing ($\grave{X}$) and upgoing ($\acute{X}$) waves, respectively). For internal multiples (IM), the first number of subscript is the order of internal multiples, and the second number of subscript is related to the number of S-wave ray-path, using same criteria as described for primaries. For example, IM^S_{22} includes all second order internal multiples received in S-wave component which involve S-wave travel-paths, i.e., $\grave{P}\grave{P}\acute{P}\grave{P}\acute{P}\grave{P}\acute{S}\acute{S}$, $\grave{P}\grave{P}\acute{P}\grave{P}\acute{S}\acute{P}\acute{S}$,$\grave{P}\grave{P}\acute{P}\grave{S}\grave{P}\acute{P}\acute{S}$,$\grave{P}\grave{P}\acute{P}\grave{S}\acute{P}\grave{P}\acute{S}$,$\grave{P}\grave{P}\acute{S}\grave{P}\acute{P}\grave{P}\acute{S}$, and $\grave{P}\grave{S}\acute{P}\grave{P}\acute{P}\grave{P}\acute{S}$.

Input preparation for $k-z$ domain using elastic stolt migration

Before performing the elastic stolt migration on a shot profile, we first calculated the angular frequency in function of vertical wavenumber $\omega(k_z)$ and its Jacobian expression. In wavenumber manner, the result is shown in Figure 3. Figure 3a and 3c are $\omega(k_z)$ and its Jacobian $\mathrm{d}\omega/\mathrm{d}k_z$ obtained from P-P component, Figure 3b and 3d are for P-SV component. Compared to P-P component, the $\omega(k_z)$ of P-SV component is not an exact smooth function which leads to the outlier values at small values of k_z. And the distribution of the outlier value becomes wider along with increasing wavenumber k_x. This outlier values may generate or even destroy the image of P-SV reflection. With two constant background velocity α and β, the elastic stolt migration is performed by re-griding data into k_z and multiplying with its related Jacobian function, then inverse transferring data from k_z to pseudo-depth z.

Figure 4 shows migrated images $R(k_h, z)$ both for P-P and P-SV reflections which are inputs for $k-z$ domain multicomponent prediction with multiplied weight factor $-2i\nu_s$. A clear image of P-P reflection is generated using elastic stolt migration with constant velocity. However, for P-SV reflection, there are some aliasing appear at the low pseudo-depth and the amplitudes of events at deep pseudo-depth are incorrect. These aliasing and miscalculated amplitudes will be big obstacles in the prediction process. Compare these two images, two primary events reflected by the 1st reflector $\grave{P}\acute{P}$ and $\grave{P}\acute{S}$ are migrated into the same pseudo-depth along with increasing wavenumber k_h.

To intuitively analyze the migrated images, the final step of elastic stolt migration is performed by stacking over k_h to achieve a single trace for a shot profile. We also transferred data from offset-time domain to offset-pseudo-depth domain by stretching P-P component with a constant velocity α and stretching P-SV component with a velocity $2\alpha\beta/(\alpha+\beta)$ and overlay the migrated traces at the zero-offset. The result is shown in Figure 5. As we concluded previously, events in the migrated trace of P-P component are well matched to the stretched zero-offset trace, the aliasing events at lower pseudo-depth and incorrect amplitudes at deeper pseudo-depth appear in the migrated P-SV trace. These migrated traces and stretched zero-offset traces indicate that the elastic stolt migration with two constant velocities successfully migrated the primary events generated by 1st interface into the same pseudo-depth, however, it is failed to migrated those primary reflected by 2nd reflector into the same pseudo-depth. This means the elastic stolt migration in wavenumber with two constant velocity is not suitable for the input preparation of multicomponent prediction algorithm.

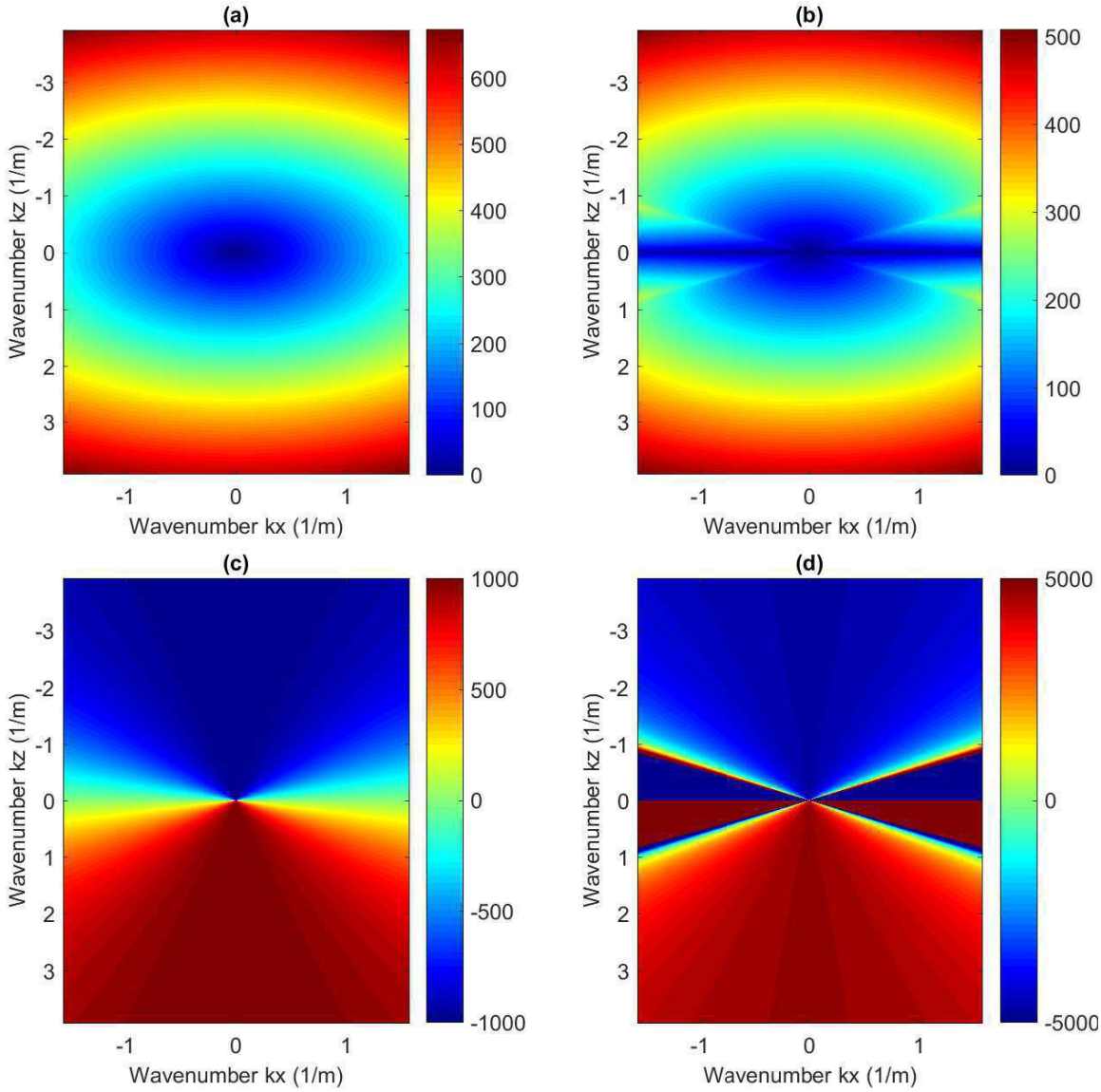

FIG. 3. The angular frequency in function of vertical wavenumber $\omega(k_z)$ and its Jacobian expression in the manner of wavenumber. (a) $\omega(k_z)$ for P-P reflection. (b) $\omega(k_z)$ for P-SV reflection. (c) Jacobian of $\omega(k_z)$ for P-P component. (d) Jacobian of $\omega(k_z)$ for P-SV component.

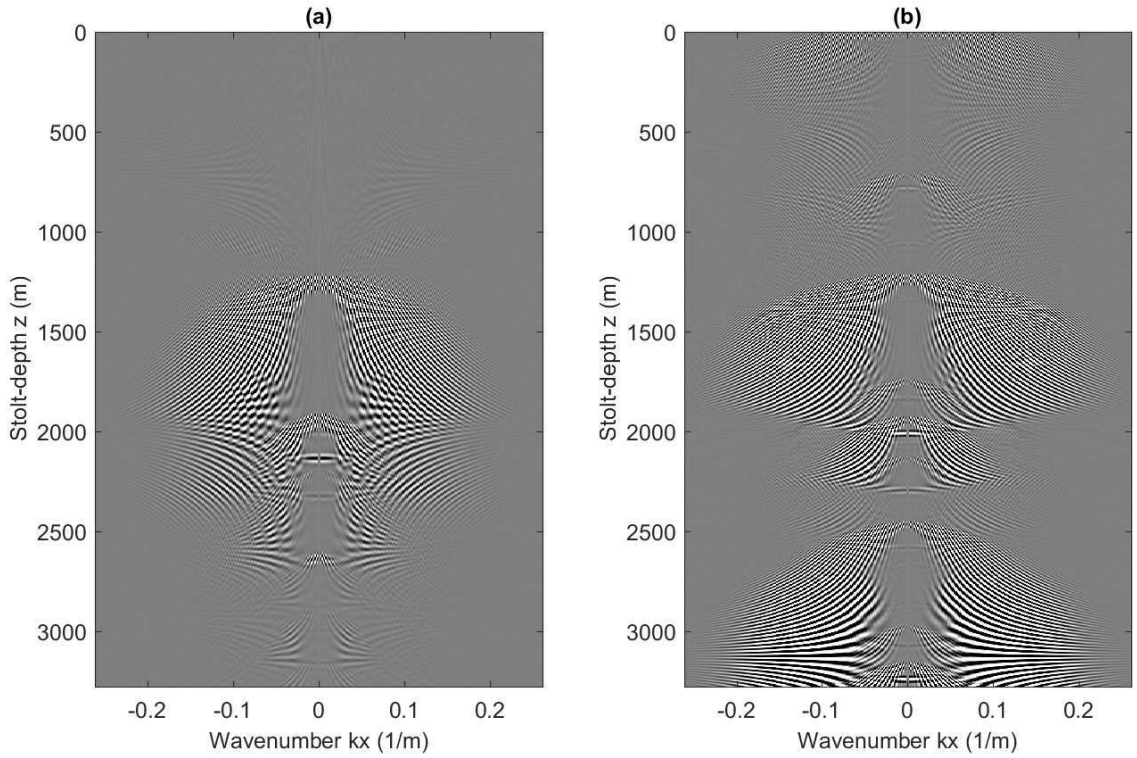

FIG. 4. The migrated image $R(k_h, z)$ using elastic stolt migration with two constant velocity. (a) The image $R(k_h, z)$ for P-P reflection. (b) The image $R(k_h, z)$ for P-SV reflection.

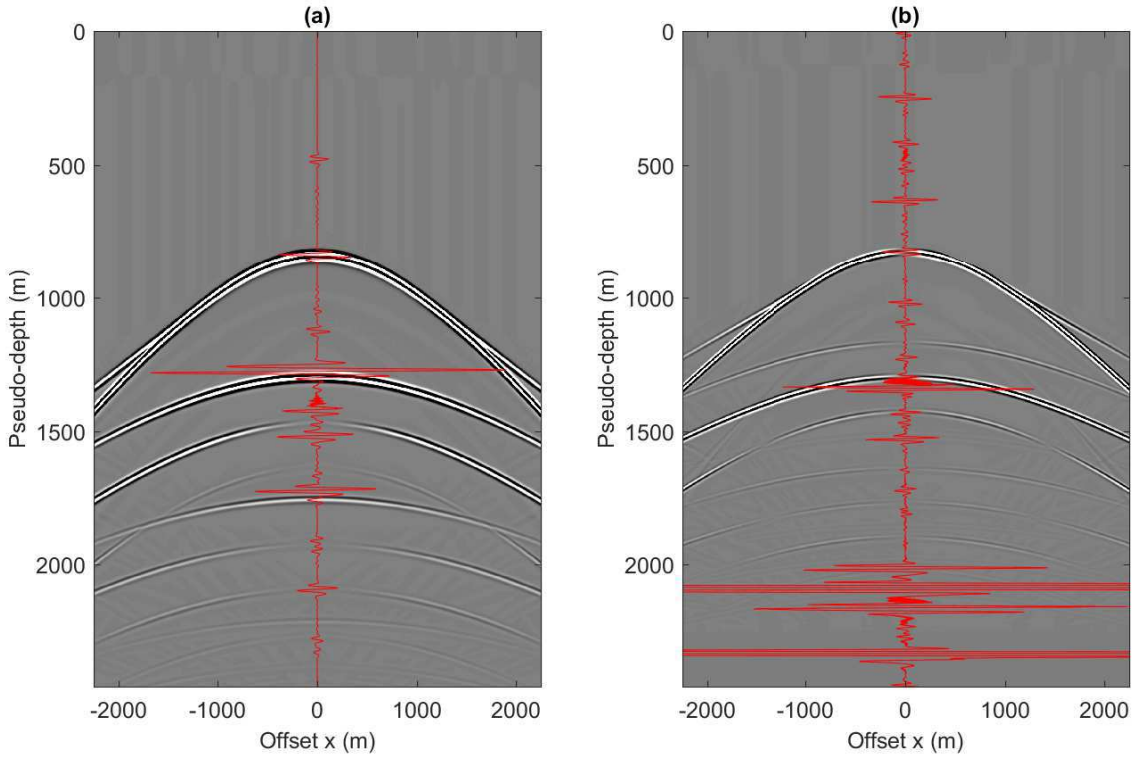

FIG. 5. The migrated traces for a shot file $R(z)$ using elastic stolt migration with two constant velocity and the stretched data in offset-pseudo-dept domain. (a) The migrated trace $R(z)$ is overlapped on stretched P-P component at zero-offset. (b) The migrated $R(z)$ is overlapped on stretched P-SV component at zero-offset.

Input preparation for $p-z$ domain using elastic stolt migration

According to the acoustic cases, compared to (k,z) domain, the implementation of internal multiple prediction in (p,z) domain has some advantages due to the convergent distribution of input along with the horizontal slowness instead of wavenumber. Therefore, to take its advantages, we also implemented elastic stolt migration in perspective of horizontal slowness to obtained the inputs of multicomponent prediction in (p,z) domain.

The angular frequency in function of wavenumber $\omega(k_z)$ with respect to the horizontal slowness and its Jacobian expression $\mathrm{d}\omega/\mathrm{d}k_z$ are computed and plotted in Figure 6. Unlikely in wavenumber domain, the angular frequency $\omega(k_z,z)$ of P-P and P-SV components along with horizontal slowness shown in Figure 6a and 6b are varying smoothly without any outliers. Same merits honour in Jacobian matrices shown in Figure 6c and 6d.

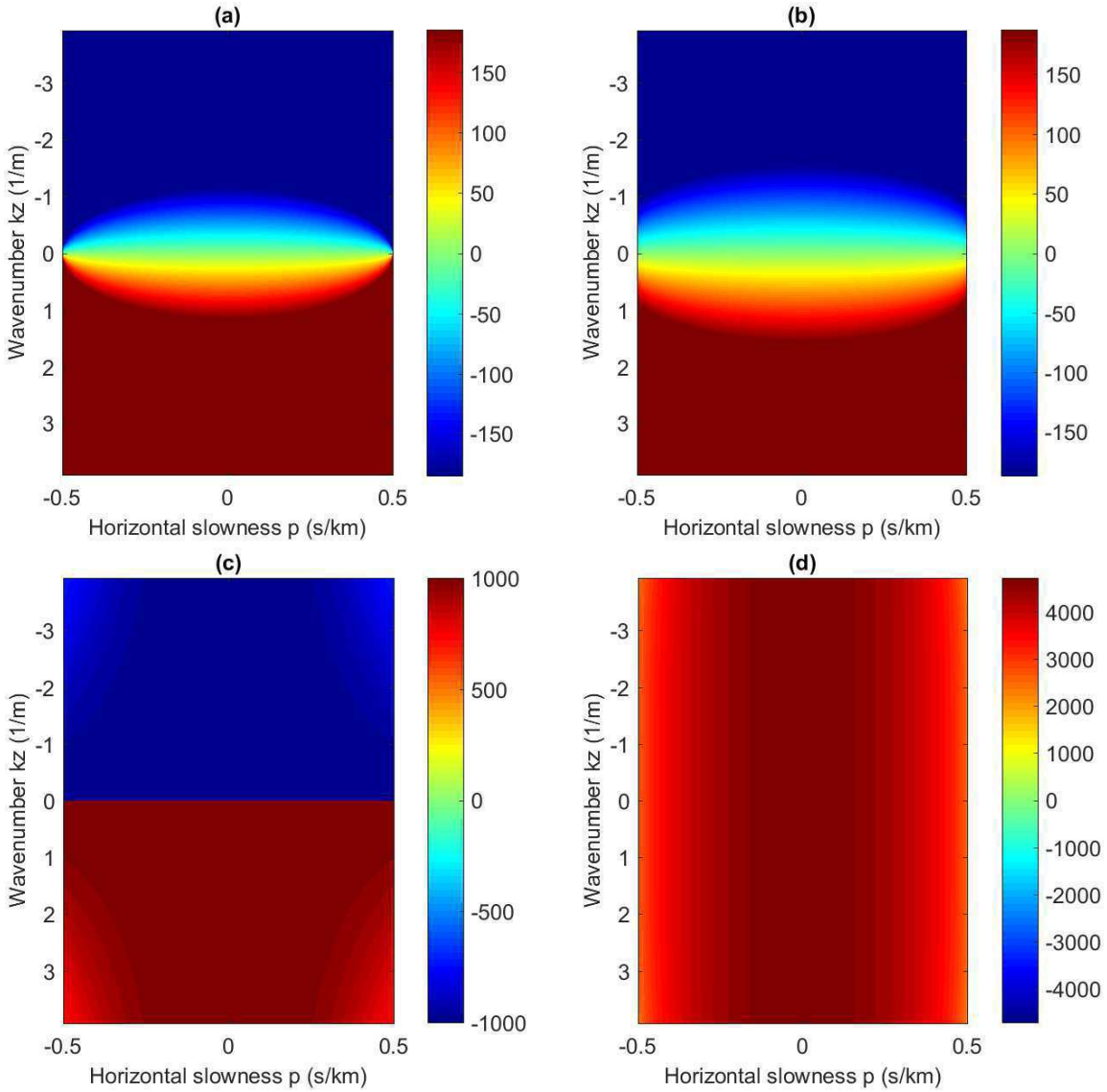

FIG. 6. The angular frequency in function of vertical wavenumber $\omega(k_z)$ and its Jacobian expression in the manner of horizontal slowness. (a) $\omega(k_z)$ for P-P reflection. (b) $\omega(k_z)$ for P-SV reflection. (c) Jacobian of $\omega(k_z)$ for P-P component. (d) Jacobian of $\omega(k_z)$ for P-SV component.

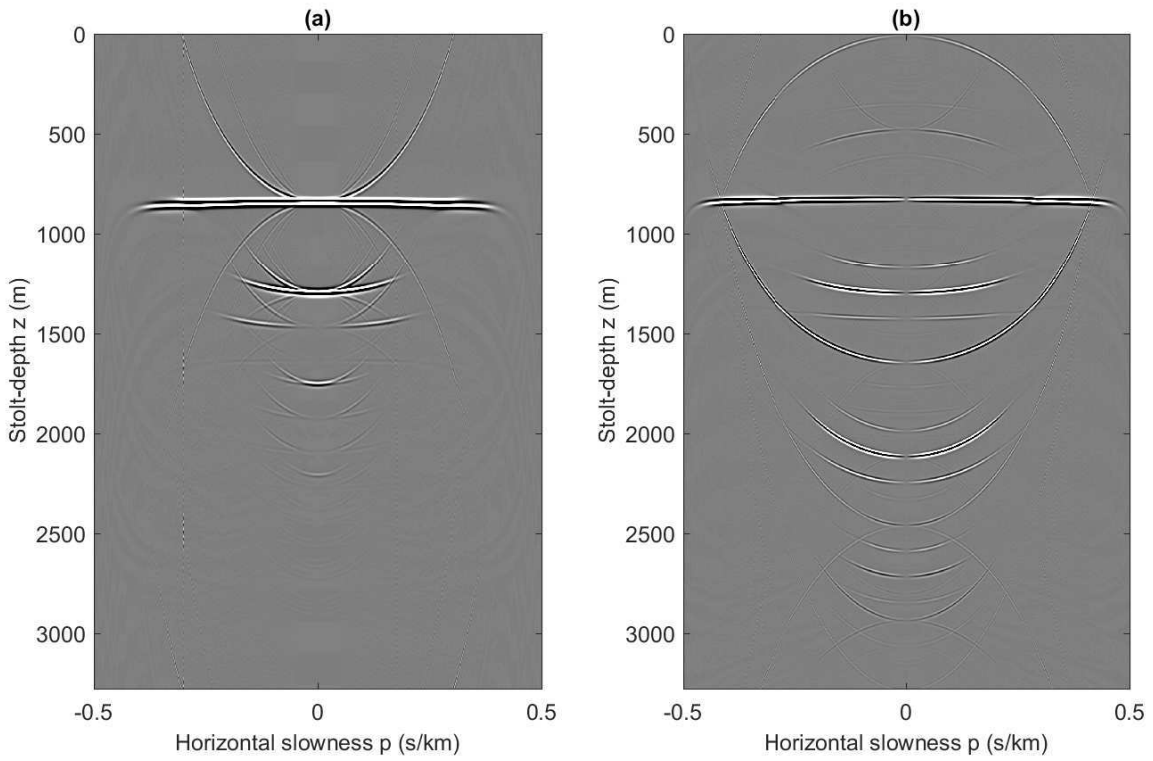

FIG. 7. The migrated image $R(p, z)$ using elastic stolt migration with two constant velocity. (a) The image $R(p, z)$ for P-P reflection. (b) The image $R(p, z)$ for P-SV reflection.

By replacing the wavenumber k_h, the elastic stolt migration with respect to horizontal slowness is also applied. The migrated images of P-P and P-SV reflections of a shot profile due to a P-wave source only are plotted in Figure 7, with multiplied by weight factor $-2iq_s$ which are inputs if the multicomponent prediction is implemented in (p, z) domain. It's obvious that there are up-and-down hyperbola aliasing around each migrated event in P-P images (Figure 7a), and ellipse aliasing are shown in migrated image of P-SV reflection (Figure 7b). These aliasing events are fatal to the multicomponent prediction as non-desired lower-higher-lower combinations are created by them. However, we cannot conclude that elastic stolt migration related to horizontal slowness does not works because $R(p, z)$ shown in Figure 7 is not the eventual result of the elastic stolt migration.

By stacking over p, the final migrated traces for P-P and P-SV reflections to a single shot profile can be achieved, as red traces shown in Figure 8. To examine the result of elastic stolt migration, the plane wave data were transferred into pseudo-depth using time-stretching with two constant velocities (i.e., α for P-P component; $2\alpha\beta/(\alpha + \beta)$ for P-SV component). The final migrated traces are overlay at traces $p = 0$. All events in migrated traces are well matched with traces $p = 0$. Similar to elastic stolt migration in wavenumber, two primaries by 1st interface are migrated to the same pseudo-depth, but elastic stolt migration with horizontal slowness is still failed to migrated those events by 2nd interface to the same pseudo-depth.

It's worth to note that both time-stretching method and elastic stolt migration yield the same result for prediction algorithm because all sub-events have a similar relative pattern.

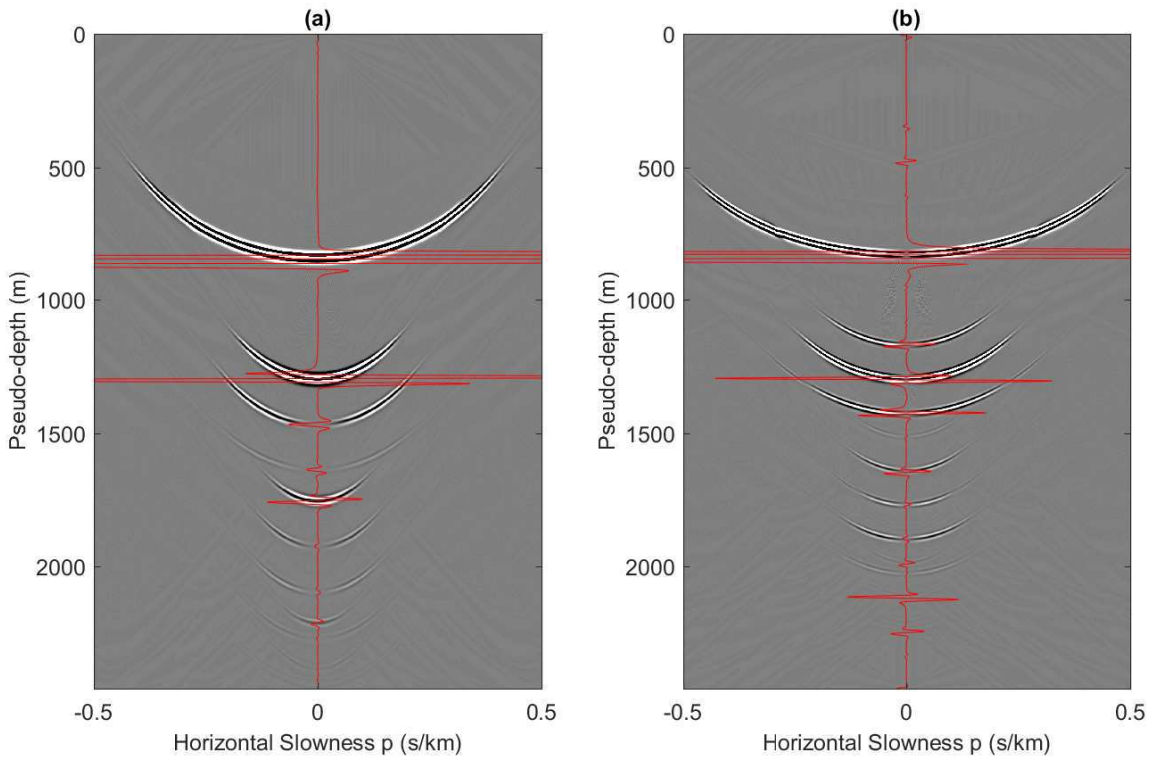

FIG. 8. The migrated traces for a shot file $R(z)$ using elastic stolt migration with two constant velocity and the stretched plane-wave data in (p, z) domain. (a) The migrated trace $R(z)$ is overlapped on stretched P-P component at trace $p = 0$. (b) The migrated $R(z)$ is overlapped on stretched P-SV component at trace $p = 0$.

Even more, the time-stretching method offers a preciser input (without aliasing) in a simpler and faster way. For these reasons, in this paper, the multicomponent prediction will not be implemented with the input created by elastic stolt migration.

Input preparation for $p - \tau$ domain with modified integral limits

The plane-wave domain prediction with time-stretched inputs (shown in Figure 8) is equivalent to the prediction by modified integral limits using equation 6 with weighted traditional $\tau - p$ transformed data as input (shown in Figure 9). Another option to modify integral limits for plane-wave prediction algorithm is delineated in equation 7 using best-fitting velocity model achieved by high-resolution hyperbolic radon transform.

The aim of high-resolution hyperbolic radon transform for prediction is to achieve the best-fitting velocity for each event by cast it into an inversion problem. And the amplitude of the radon panel does not matter since the corresponded velocity of the bright-spot in lateral axis is the only desired parameter. Therefore, we recommend to apply a gain filter along with time-axis to achieve conspicuous bright-spots at large vertical traveltime by enhancing their amplitudes in offset-time domain. The gain filter could be multiplying traces by a factor, such as t^{tpow}.

In the paper written by Trad et al. (2002), the author introduced a non-uniform velocity grid to achieve a sparse radon panel. However, a non-uniform Δv increases the risk of

picking the best-fitting velocity in radon panel. To get a more precise best-fit, we will use a small uniform velocity interval Δv. An uniform velocity interval is not the best option for obtaining a sparse model, however, it is a trade-off we have to make.

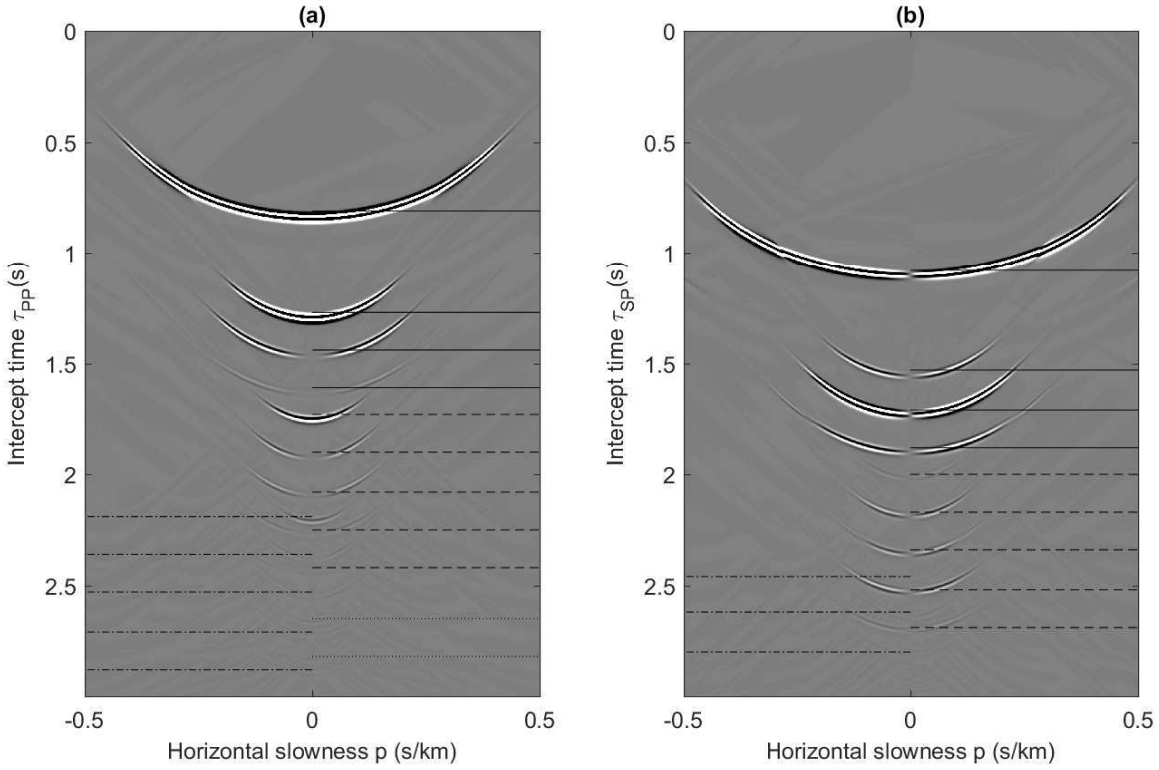

FIG. 9. Linear radon panel of data shown in Figure 2.(a) P-wave component in linear radon space. (b) SV-wave component in linear radon space.

As discussed, the time domain hyperbolic radon transform was solved by re-weighted least square method with an uniform velocity interval $\Delta v = 20m/s$. The transferred hyperbolic radon panels for -P- and P-SV reflections are drawn in Figure 10. The lateral coordinate of each red circle indicates best-fitting velocity (v_s) for each hyperbola event. And the vertical coordinate of each red circle denotes the two-way zero-offset traveltime (τ_0) of each event. These picked (v_s, τ_0) is remapping into linear radon space using elliptical radon transform. Here, we only picked best-fit velocity for first nine events.

Best-fitting velocity models for P-P and P-SV components in linear radon space are shown in Figure 11. In multicomponent prediction scheme with best-fitting velocity, the input will be the traditional linear radon $(\tau - p)$ transformed data multiplying its corresponded weighting factor $-i2q_s^X$. Here, X denotes the wave-mode on source side. And equation 7 using velocity shown in Figure 11 is the criteria for selecting possible combinations satisfying lower-higher-lower relationship. To pre-examine the picked best-fitting velocity, we also plotted the matching between velocity model and the $\tau - p$ transformed data in linear radon space, shown in Figure 12.

Again, as Part I indicated, multicomponent prediction with best-fitting velocity has been improved and offered a better solution for identifying lower-higher-lower relationship, however, it cannot handle the multiple prediction inter-reflected by thin layer. In other

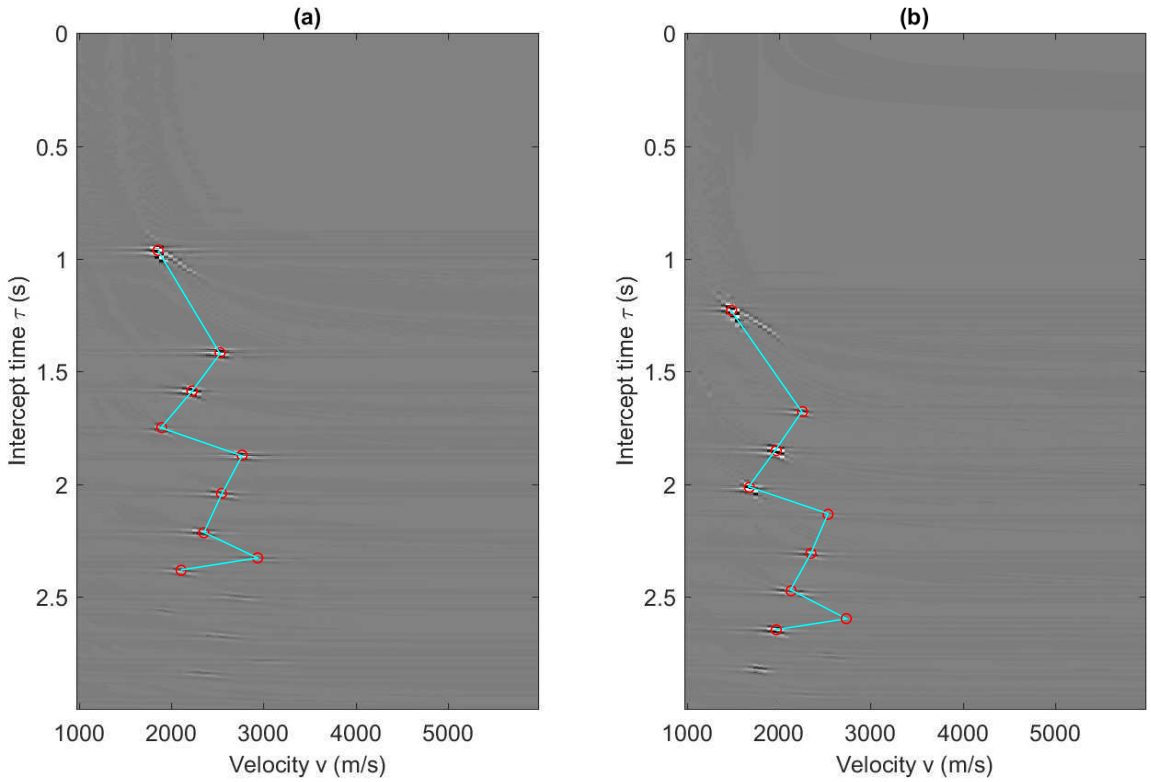

FIG. 10. Hyperbolic radon panel of data shown in Figure 2. Red circles indicate the bright spot pricked for each event. (a) P-wave component in hyperbolic radon space. (b) SV-wave component in hyperbolic radon space.

words, a relative large search parameter is required for multicomponent prediction with best-fitting velocity only using modified integral limits. Besides that, we also noted that a cross-validated modified integral limits using both time-stretching and best-fitting velocity may allow a smaller ϵ to ascertain the lower-higher-lower criteria.

SYNTHETIC: PREDICTION AND DISCUSSION

Since those aliasing events of inputs generated by elastic stolt migration gravely disordered the lower-higher-lower relationship of subevents, there is no point to implement the multicomponent prediction with elastic stlot migrated inputs in k, z and in p, z domain. Besides, prediction with modified integral limits by time-stretching is equivalent to prediction with stolt-migrated inputs or with time-stretched inputs. Therefore, in this section, we will only perform the multicomponent prediction with modified integral limits, which provided by time-stretching, best-fitting velocity, and the intersection of time-stretching and best-fitting velocity.

Prediction with time-stretching condition

By considering the linear radon panel (shown in Figure 9) as the input, we first implemented the prediction with time-stretched integral limits (equation 6). The chosen epsilon is 96 ms. Two constant velocities are $\alpha = 2000m/s$ and $\beta = 1200m/s$. The predicted result is shown in Figure 13. According to the labels in Figure 13, all internal multiples are

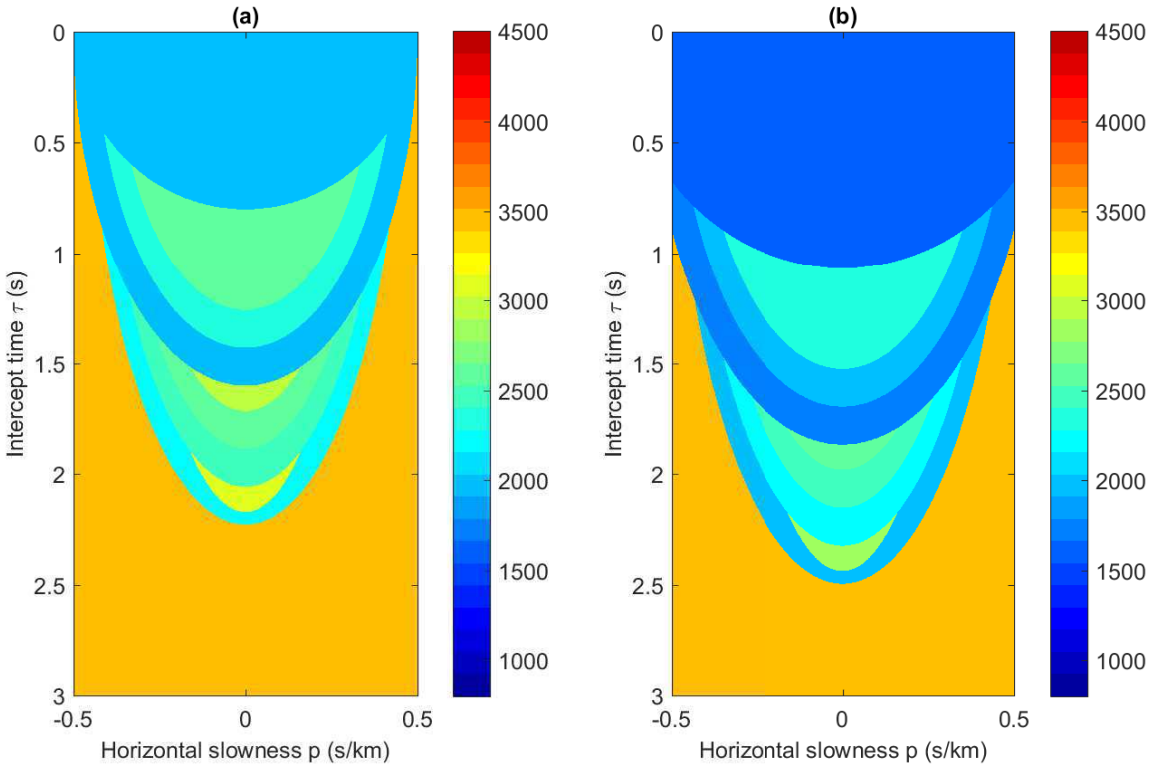

FIG. 11. Best fitting velocity models in linear radon space picked from Figure 10. (a) Velocity for P-wave component . (b) Velocity for SV-wave component.

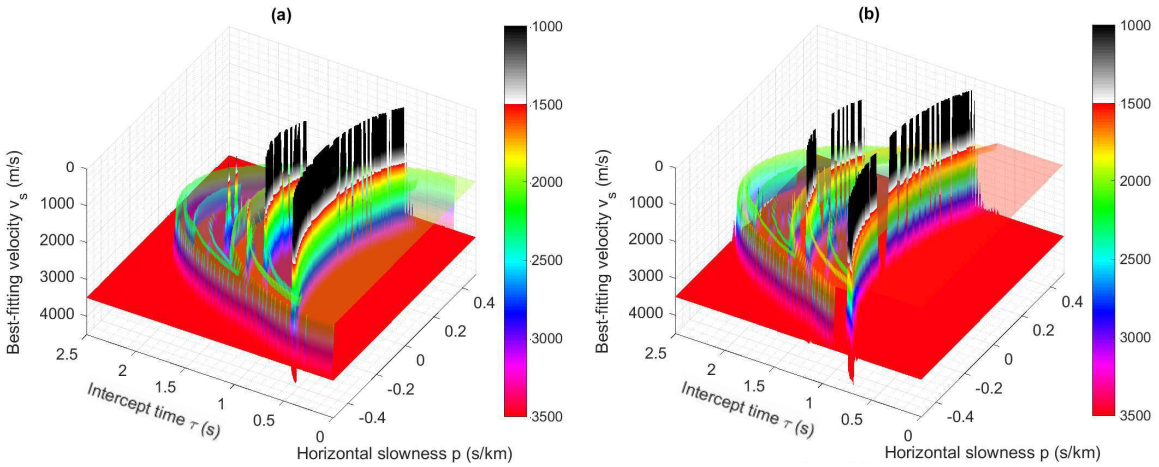

FIG. 12. The matching between best-fit velocity and linear radon panel. (a) Velocity matching for P-wave component . (b) Velocity matching for SV-wave component.

successfully predicted, but along with some undesired events. For example, two primary events are also predicted at the near-offset in P-P component, and one primary appeared in prediction of P-SV component. These undesired events are generated by false combinations satisfying lower-higher-lower relationship because the time-stretching method are failed to shift those primaries reflected by 2nd reflector at the same pseudo-depth. We enumerate one possible lower-higher-lower combination for generating each primary of Figure 13 and they are drawn in Figure 14 (The lower-higher-lower relationship of sub-events in each combinations are verified by the analytical analysis in Part I). The prediction in Figure 13

has again validated our conclusion that elastic stolt migration with two constant velocities is not the solution for the input preparation of multicomponent internal multiple prediction.

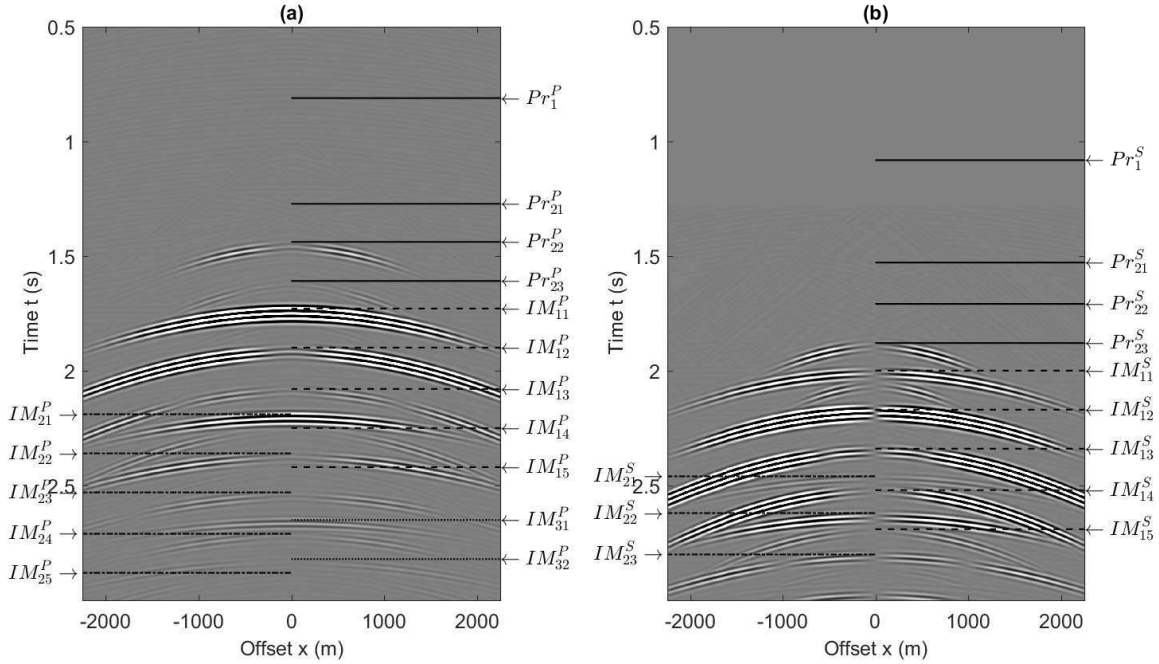

FIG. 13. Multicomponent internal multiple prediction using time-stretched condition with $\epsilon = 96ms$. (a) Prediction for P-wave component . (b) Prediction for SV-wave component.

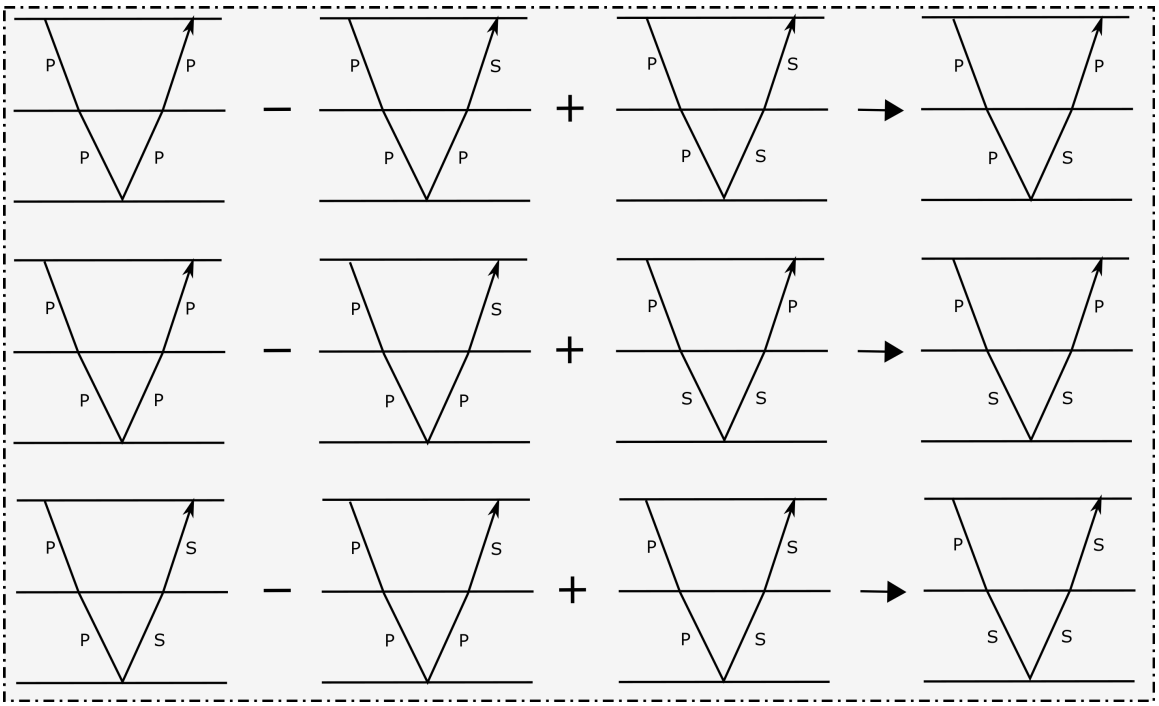

FIG. 14. One possible lower-higher-lower (LHL) combination for each primary shown in Figure 13. The 1st row is one of combinations satisfying LHL for $\grave{P}\grave{P}\acute{S}\acute{P}$. The 2nd row is one of combination for $\grave{P}\grave{S}\acute{S}\acute{P}$. The 3rd row is one of combination for $\grave{P}\grave{S}\acute{S}\acute{S}$.

Prediction with best-fitting condition

Based on the analysis in Part I (Figure 3b, Part I), the largest mismatch pseudo-depth of those events reflected by 2nd interface is over $450m$ (i.e., $\tau = 450ms$ in the two-way vertical traveltime). It's meaningless to examine the prediction using time-stretching condition only with a larger ϵ value. However, the largest mismatch pseudo-depth (Figure 3c, Part I) is 165m (i.e., $\tau = 165ms$ in two-way vertical traveltime). Here, we implemented the multicomponent prediction using best-fitting velocity model shown in Figure 11 with a constant $\epsilon = 200ms$, which is a little bit smaller than the sum of wavelet-bandwidth $(96ms)$ and the mismatch two-way vertical traveltime $(165ms)$.

The prediction of P-P and P-SV components are shown in Figure 15. It's fair to say that the best-fitting prediction algorithm produces a much better result comparing with the prediction with time-stretching. All primary events are well eliminated both in P-P and P-SV modes, and elastic internal multiples are predicted in each orders. One of the shortcoming in this approach is that it requires a large ϵ. And even more, in practical cases, it's no possible to obtained the largest mismatch two-way vertical traveltime. Here, we compromise to chose the two-times of the wavelet-bandwidth as the ϵ value.

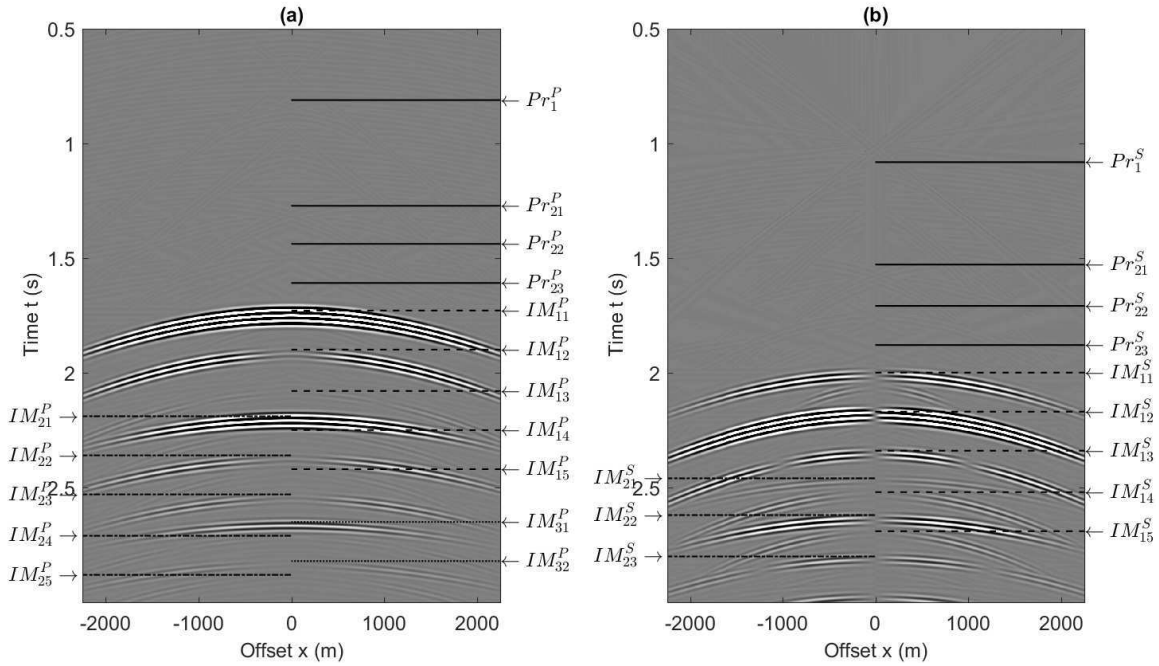

FIG. 15. Multicomponent internal multiple prediction using best-fitting velocity with $\epsilon = 200ms$. (a) Prediction for P-wave component . (b) Prediction for SV-wave component.

Prediction with cross-validate condition

To reduce the ϵ dependency of prediction algorithm, we also examine the multicomponent prediction using a cross-validate condition generated by time-stretching and best-fitting velocity model. The implementation was performed with a $\epsilon = 96ms$. Figure 16 shows the final predicted internal multiples for P-P and P-SV components. As expected, even with a smaller search parameter, all primary events are well eliminated and all internal multiples are predicted at correct traveltime.

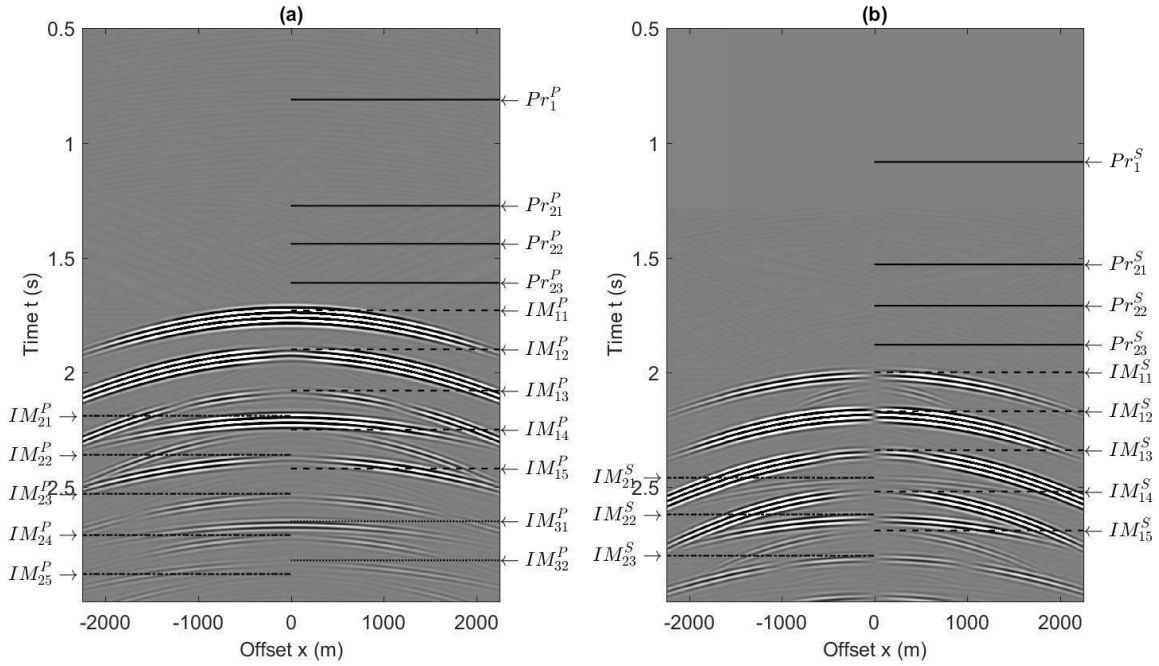

FIG. 16. Multicomponent internal multiple prediction using cross-validate condition of best-fitting velocity and time-stretching with $\epsilon = 96ms$. (a) Prediction for P-wave component . (b) Prediction for SV-wave component.

With the analysis of comparison between those predicted results, we can summary that, first, elastic stolt-migration with two constant background velocity does not generate the appropriate input for the prediction; second, time-stretching methods create the equivalent inputs, but noise-free, as elastic stolt migration does, which is also not suitable to multi-component prediction; third, prediction with best-fitting velocity model can produce an acceptable results, however, it requires a large constant search parameter ϵ which may increase the risk of missing short-leg internal multiple prediction; fourth, the cross-validate condition offers a better solution to select the lower-higher-lower combinations and also allows a regular search parameter for multicomponent prediction.

CONCLUSIONS

Identifying the lower-higher-lower relationship of sub-events is an essential step of inverse scattering series internal multiple prediction. Compared to acoustic prediction algorithm, selecting appropriate combinations satisfying lower-higher-lower relationship in multicomponent internal multiple prediction becomes to be more difficult and dependent on the input preparation due to the wave-mode conversion. Variant methods for input preparation are discussed. With the quantitatively analysis, the elastic stolt migration with constant background velocity both in (k, z) domain and in (p, z) domain has been proven to be an inappropriate solution for multicomponent prediction because it generates aliasing and fails to migrated primaries into the depth they should be. The time-stretching method can generate an equivalent but cleaner input as the elastic stolt migration does, however, it also has the same issue of shifting primary into its correct two-way vertical traveltime. Using high-resolution radon transform, the obtained best-fitting velocity model has the ability to provide a best approximation of the lower-higher-lower relationship in actual depth

but requires a large constant search parameter. Comparing best-fitting approach with time-stretching method, we note that the opposite sorting are generated by these two approaches. Therefore, the cross-validate condition by these two methods may reduce the dependency of the search parameter.

To examine our conclusion, a synthetic data is applied to multicomponent prediction. As expected, the predicted results indicate that prediction with time-stretching only will failed to eliminate all primary events because of the large mismatch between primaries. The best-fitting velocity model with a large constant ϵ can produce the correct prediction of multicomponent internal multiple. However, it's hard to know if the ϵ is suitable in piratical. The prediction with a cross-validate generated by time-stretching and best-fitting velocity provides the best predicted results which also allows a regular ϵ.

ACKNOWLEDGEMENTS

We thank the sponsors of CREWES for continued support. This work was funded by CREWES industrial sponsors and NSERC (Natural Science and Engineering Research Council of Canada) through the grant CRDPJ 461179-13.

REFERENCES

Behura, J., Wapenaar, K., and Snieder, R., 2014, Autofocus imaging: Image reconstruction based on inverse scattering theory: Geophysics, **79**, No. 3, A19–A26.

Berkhout, A., 2006, Seismic processing in the inverse data space: Geophysics, **71**, No. 4, A29–A33.

Berkhout, A., and Verschuur, D., 2005, Removal of internal multiples with the common-focus-point (cfp) approach: Part 1âĂŤexplanation of the theory: Geophysics, **70**, No. 3, V45–V60.

Berkhout, A., and Verschuur, D., 2006, Imaging of multiple reflections: Geophysics, **71**, No. 4, SI209–SI220.

Coates, R., and Weglein, A., 1996, Internal multiple attenuation using inverse scattering: Results from prestack 1 & 2d acoustic and elastic synthetics, *in* 1996 SEG Annual Meeting, Society of Exploration Geophysicists.

Innanen, K. A., 2017, Time and offset domain internal multiple prediction with non-stationary parameters: Geophysics, accepted.

Kelamis, P. G., Erickson, K. E., Verschuur, D. J., and Berkhout, A., 2002, Velocity-independent redatuming: A new approach to the near-surface problem in land seismic data processing: The Leading Edge, **21**, No. 8, 730–735.

Li, Z., Li, Z., Wang, P., and Zhang, M., 2016, Reverse time migration of multiples based on different-order multiple separation: Geophysics, **82**, No. 1, S19–S29.

Liu, Y., Chang, X., Jin, D., He, R., Sun, H., and Zheng, Y., 2011, Reverse time migration of multiples for subsalt imaging: Geophysics, **76**, No. 5, WB209–WB216.

Luo, Y., Zhu, W., Kelamis, P. G. et al., 2007, Internal multiple reduction in inverse-data domain: SEG Expanded Abstracts. San Antonio:[sn], 125–129.

Malcolm, A. E., De Hoop, M. V., and Ursin, B., 2011, Recursive imaging with multiply scattered waves using partial image regularization: A north sea case study: Geophysics, **76**, No. 2, B33–B42.

Malcolm, A. E., Ursin, B., and Maarten, V., 2009, Seismic imaging and illumination with internal multiples: Geophysical Journal International, **176**, No. 3, 847–864.

Matson, K. H., 1997, An inverse scattering series method for attenuating elastic multiples from multicomponent land and ocean bottom seismic data: Ph.D. thesis, University of British Columbia.

Slob, E., Wapenaar, K., Broggini, F., and Snieder, R., 2014, Seismic reflector imaging using internal multiples with marchenko-type equations: Geophysics, **79**, No. 2, S63–S76.

Sun, J., and Innanen, K. A. H., 2015, 1.5 d internal multiple prediction in the plane wave domain: CSEG Geoconvention.

Sun, J., and Innanen, K. A. H., 2016a, Implementation of predicting elastic internal multiples based on inverse scattering series: synthetic results: CREWES Research Report, **28**, 1–15.

Sun, J., and Innanen, K. A. H., 2016b, Interbed multiple prediction on land: which technology, and which domain?: CSEG recorder, **41**, No. 8, 24–29.

Sun, J., and Innanen, K. A. H., 2016c, Inverse-scattering series internal-multiple prediction in the double tau-p domain, *in* SEG Technical Program Expanded Abstracts 2017, Society of Exploration Geophysicists, 4555–4560.

Trad, D. O., Ulrych, T. J., and Sacchi, M. D., 2002, Accurate interpolation with high-resolution time-variant radon transforms: Geophysics, **67**, No. 2, 644–656.

Weglein, A. B., 2016, Multiples: Signal or noise?: Geophysics, **81**, No. 4, V283–V302.

Weglein, A. B., Gasparotto, F. A., Carvalho, P. M., and Stolt, R. H., 1997, An inverse-scattering series method for attenuating multiples in seismic reflection data: Geophysics, **62**, No. 6, 1975–1989.

Zou, Y., and Weglein, A. B., 2015, An internal-multiple elimination algorithm for all first-order internal multiples for a 1d earth, *in* SEG Technical Program Expanded Abstracts 2015, Society of Exploration Geophysicists, 4408–4412.

Zuberi, M. A. H., and Alkhalifah, T., 2014, Generalized internal multiple imaging: Geophysics, **79**, No. 5, S207–S216.